

**Accepted Article Preview: Published ahead of advance online publication**



**Phase recovery and holographic image reconstruction using deep learning in neural networks**

Yair Rivenson, Yibo Zhang, Harun Günaydın, Da Teng and Aydogan Ozcan

Cite this article as: Yair Rivenson, Yibo Zhang, Harun Günaydın, Da Teng and Aydogan Ozcan. Phase recovery and holographic image reconstruction using deep learning in neural networks. *Light: Science & Applications* accepted article preview 13 October 2017; doi: 10.1038/lssa.2017.141

This is a PDF file of an unedited peer-reviewed manuscript that has been accepted for publication. NPG are providing this early version of the manuscript as a service to our customers. The manuscript will undergo copyediting, typesetting and a proof review before it is published in its final form. Please note that during the production process errors may be discovered which could affect the content, and all legal disclaimers apply.

Received 21 June 2017; revised 5 October 2017; accepted 11 October 2017;  
Accepted article preview online 13 October 2017

## Phase recovery and holographic image reconstruction using deep learning in neural networks

Yair Rivenson<sup>1,2,3,†</sup>, Yibo Zhang<sup>1,2,3,†</sup>, Harun Günaydın<sup>1</sup>, Da Teng<sup>1,4</sup>, Aydogan Ozcan<sup>1,2,3,5\*</sup>

### Affiliations:

<sup>1</sup>Electrical Engineering Department, University of California, Los Angeles, CA, 90095, USA.

<sup>2</sup>Bioengineering Department, University of California, Los Angeles, CA, 90095, USA.

<sup>3</sup>California NanoSystems Institute (CNSI), University of California, Los Angeles, CA, 90095, USA.

<sup>4</sup>Computer Science Department, University of California, Los Angeles, CA, 90095, USA

<sup>5</sup>Department of Surgery, David Geffen School of Medicine, University of California, Los Angeles, CA, 90095, USA.

\*Correspondence: [ozcan@ucla.edu](mailto:ozcan@ucla.edu)

Address: 420 Westwood Plaza, Engineering IV Building, UCLA, Los Angeles, CA 90095, USA

Tel.: +1 (310) 825-0915

Fax: +1 (310) 206-4685

†Equally contributing authors.

**Abstract**

Phase recovery from intensity-only measurements forms the heart of coherent imaging techniques and holography. In this study, we demonstrate that a neural network can learn to perform phase recovery and holographic image reconstruction after appropriate training. This deep learning-based approach provides an entirely new framework to conduct holographic imaging by rapidly eliminating twin-image and self-interference-related spatial artifacts. This neural network-based method is fast to compute and reconstructs phase and amplitude images of the objects using only one hologram, requiring fewer measurements in addition to being computationally faster. We validated this method by reconstructing the phase and amplitude images of various samples, including blood and Pap smears and tissue sections. These results highlight that challenging problems in imaging science can be overcome through machine learning, providing new avenues to design powerful computational imaging systems.

**Keywords:** holography, deep learning, neural networks, phase recovery, machine learning

## Introduction

Opto-electronic sensor arrays, such as charge-coupled devices (CCDs) or complementary metal-oxide-semiconductor (CMOS)-based imagers, are only sensitive to the intensity of light; therefore, phase information of the objects or the diffracted light waves cannot be directly recorded using such imagers. Phase recovery from intensity-only measurements has emerged as an important field to recover this lost phase information in the detection process, enabling the reconstruction of the phase and amplitude images of specimen using various approaches<sup>1-13</sup>. In fact, Gabor's original in-line holography system<sup>14</sup>, where the diffracted light from the object interferes with the background light that is directly transmitted, is an important example where phase recovery is required to separate the twin-image and self-interference-related spatial artifacts from the real image of the sample. In various implementations, to improve the performance of the phase recovery and image reconstruction processes, additional intensity information is recorded, e.g., by scanning the illumination source aperture<sup>15-18</sup>, sample-to-sensor distance<sup>19-23</sup> (in some cases referred to as out-of-focus imaging<sup>24</sup>), wavelength of illumination<sup>25,26</sup>, or phase front of the reference beam<sup>27-30</sup>, among other methods<sup>31-36</sup>. All these methods utilize additional physical constraints and intensity measurements to robustly retrieve the missing phase information based on an analytical and/or iterative solution that satisfies the wave equation. Some of these phase retrieval techniques have enabled discoveries in different fields<sup>37-40</sup>.

In this paper, we report a convolutional neural network-based method, trained through deep learning<sup>41,42</sup>, that can perform phase recovery and holographic image reconstruction using a *single* hologram intensity. Deep learning is a machine learning technique that uses a multi-layered artificial neural network for data modeling, analysis and decision making and has shown considerable success in areas where large amounts of data are available. Deep learning has recently been applied to solving inverse problems in imaging science such as in super-resolution<sup>43,44</sup>, acceleration of the image acquisition speed of computed tomography (CT)<sup>45</sup>, magnetic resonance imaging (MRI)<sup>46</sup>, photoacoustic tomography<sup>47</sup>, and holography.<sup>48,49</sup>

In this work, we used deep learning to rapidly perform phase recovery and reconstruct complex-valued images of specimen using a single intensity-only hologram. This process is very fast, requiring approximately 3.11 sec on a graphics processing unit (GPU)-based laptop computer to recover the phase and amplitude images of a specimen over a field of view of 1 mm<sup>2</sup> with approximately 7.3 megapixels in each image channel (amplitude and phase). We validated this approach by reconstructing the complex-valued images of various samples, such as blood and Papanicolaou (Pap) smears as well as thin sections of human tissue samples, all of which demonstrated successful elimination of the twin-image and self-interference-related spatial artifacts that arise due to lost phase information during the hologram detection process. In other words, the convolutional neural network, after its training, learned to extract and separate the spatial features of the real image from the features of the twin-image and other undesired interference terms for both the phase and amplitude channels of the object. Remarkably, this deep learning-based phase recovery and holographic image reconstruction approach has been achieved without any modeling of light-matter interaction or wave interference. However, this does not imply that the presented approach entirely ignores the physics of light-matter interaction and holographic imaging, which is in fact statistically inferred through deep learning in the convolutional neural network by using a large number of microscopic images as the gold standard in the training phase. This training and statistical optimization of the neural network is performed once and can be considered as part of a blind

reconstruction framework that performs phase recovery and holographic image reconstruction using a single input such as an intensity-only hologram of the object. This framework introduces a myriad of opportunities to design fundamentally new coherent imaging systems and can be broadly applicable to any phase recovery problem, spanning different parts of the electromagnetic spectrum, including visible wavelengths as well as X-rays<sup>28,30,50,51</sup>.

## Results and Discussion

Our deep neural network approach for phase retrieval and holographic image reconstruction is schematically described in Fig. 1 (see also Supplementary Figs. 1-4). In this work, we chose to demonstrate the proposed framework using lens-free digital in-line holography of transmissive samples, including human tissue sections and blood and Pap smears (see Methods). Due to the dense and connected nature of these samples that we imaged, their holographic in-line imaging requires the acquisition of multiple holograms for accurate and artifact-free object recovery<sup>52</sup>. A schematic of our experimental setup is shown in Supplementary Fig. 5, where the sample is positioned very close to a CMOS sensor chip with a  $< 1$  mm sample-to-sensor distance, which provides an important advantage in terms of the sample field of view that can be imaged. However, due to this relatively short sample-to-sensor distance, the twin-image artifact of the in-line holography, which is a result of the lost phase information, is strong and severely obstructs the spatial features of the sample in both the amplitude and phase channels, as illustrated in Figs. 1-2.

The first step in our deep learning-based phase retrieval and holographic image reconstruction framework consists of “training” the neural network. This training involves learning the statistical transformation between a complex-valued image that results from the back-propagation of a *single* intensity-only hologram of the object and the same object’s image that is reconstructed using a multi-height phase retrieval algorithm (treated as the gold standard for the training phase). This algorithm uses 8 hologram intensities acquired at different sample-to-sensor distances (see Methods as well as Supplementary Information). As illustrated in Figs. 1-3, a simple back-propagation of the object’s hologram, without phase retrieval, contains severe twin-image and self-interference-related artifacts, hiding the phase and amplitude information of the object. This training/learning process (which is performed only once) results in a *fixed* deep neural network that is used to *blindly* reconstruct the phase and amplitude images of any object, free from twin-image and other undesired interference-related artifacts, using a single hologram intensity.

In our holographic imaging experiments, we used three different types of samples: blood smears, Pap smears and breast tissue sections, and separately trained three convolutional neural networks for each sample type, although the network architecture was identical in each case, as shown in Fig. 1. To avoid over-fitting the neural network, we stopped the training when the deep neural network performance on the validation image set (which is different from the training image set and the blind testing image set) began to decline. We also accordingly made the network compact and applied pooling approaches<sup>53</sup>. Following this training process, each deep neural network was *blindly* tested with different objects that were *not* used in the training or validation image sets. Figs. 1, 2 and 3 show the neural network-based blind reconstruction results for the Pap smears, breast tissue sections and blood smears. These reconstructed phase and amplitude images clearly demonstrate the success of our deep neural network-based

holographic image reconstruction approach to blindly infer artifact-free phase and amplitude images of the objects, matching the performance of the multi-height phase recovery. Table 1 further compares the structural similarity<sup>54</sup> (SSIM) of our neural network output images (using a single input hologram, i.e.,  $N_{\text{holo}} = 1$ ) against the results obtained with a traditional multi-height phase retrieval algorithm using multiple holograms (i.e.,  $N_{\text{holo}} = 2, 3, \dots, 8$ ) acquired at different sample-to-sensor distances. A comparison of the SSIM index values reported in Table 1 suggests that the imaging performance of the deep neural network using a single hologram is comparable to that of multi-height phase retrieval, closely matching the SSIM performance of  $N_{\text{holo}} = 2$  for both Pap smear and breast tissue samples and the SSIM performance of  $N_{\text{holo}} = 3$  for blood smear samples. The deep neural network-based reconstruction approach reduces the number of holograms required by 2-3 times. In addition to this reduction in the number of holograms, the computation time for holographic reconstruction using a neural network is also improved by more than 3- and 4-fold compared with those of the multi-height phase retrieval using  $N_{\text{holo}} = 2$  and  $N_{\text{holo}} = 3$ , respectively (see Table 2).

The phase retrieval performance of our neural network is further demonstrated by imaging red blood cells (RBCs) in a whole blood smear. Using the reconstructed phase images of RBCs, the relative phase delay with respect to the background (where no cells are present) is calculated to reveal the *phase integral* per RBC (given in units of  $\text{rad} \cdot \mu\text{m}^2$  - see Supplementary Information for details), which is directly proportional to the volume of each cell,  $V$ . In Fig. 3(a), we compare the phase integral values of 127 RBCs in a given region of interest, which were calculated using the phase images of the network input, the network output, and the multi-height phase recovery image obtained with  $N_{\text{holo}} = 8$ . Due to the twin-image and other self-interference-related spatial artifacts, the effective cell volume and the phase integral values calculated using the network input image demonstrated a highly random behavior. This behavior is shown as the scattered blue dots in Fig. 3(a) and is significantly improved by the network output, shown as the red dots in the same figure.

Next, to evaluate the tolerance of the deep neural network and its holographic reconstruction framework to axial defocusing, we digitally back-propagated the hologram intensity of a breast tissue section to different depths, i.e., defocusing distances within a range of  $z = [-20 \mu\text{m}, +20 \mu\text{m}]$  with  $\Delta z = 1 \mu\text{m}$  increments. After this defocusing, we then fed each resulting complex-valued image as input into the same fixed neural network, which was trained by using in-focus images at  $z = 0 \mu\text{m}$ . The amplitude SSIM index of each network output was evaluated with respect to the multi-height phase recovery image with  $N_{\text{holo}} = 8$  used as the reference (see Fig. 4). Although the deep neural network was trained with in-focus images, Fig. 4 demonstrates the ability of the network to blindly reconstruct defocused holographic images with a negligible drop in image quality across the imaging system's depth of field, which is  $\sim 4 \mu\text{m}$ .

In a digital in-line hologram, the intensity of the light incident on the sensor array can be written as

$$I(x, y) = |A + a(x, y)|^2 = |A|^2 + |a(x, y)|^2 + A^*a(x, y) + Aa^*(x, y) \quad (1)$$

where  $A$  is the uniform reference wave that is directly transmitted and  $a(x, y)$  is the complex-valued light wave that is scattered by the sample. Under plane wave illumination, we can assume that  $A$  has zero phase at the detection plane, without loss of generality, i.e.,  $A = |A|$ . For a weakly scattering object, the self-interference term  $|a(x, y)|^2$  can be ignored compared with the other terms in equation (1) because

$|a(x, y)| \ll A$ . As detailed in our Supplementary Information, none of the samples that we imaged in this work satisfies this weakly scattering assumption. More specifically, the root-mean-squared (RMS) modulus of the scattered wave was measured to be approximately 28%, 34% and 37% of the reference wave RMS modulus for breast tissue, Pap smear and blood smear samples, respectively. This is why, for in-line holographic imaging of such strongly scattering and structurally dense samples, self-interference-related terms, in addition to twin-image terms, form strong image artifacts in both the phase and amplitude channels of the sample, making it difficult to apply object support-based constraints for phase retrieval. This necessitates additional holographic measurements for traditional phase recovery and holographic image reconstruction methods such as the multi-height phase recovery approach that we used for comparison in this work. Without increasing the number of holographic measurements, our deep neural network-based phase retrieval technique can learn to separate/clean the phase and amplitude images of the objects from twin-image and self-interference-related spatial artifacts, as illustrated in Figs. 1-3. In principle, one could also use off-axis interferometry<sup>55-57</sup> to image strongly scattering samples. However, this would create a penalty in the resolution or field of view of the reconstructed images due to the reduction in the space-bandwidth product of an off-axis imaging system.

Another important property of this deep neural network-based holographic reconstruction framework is that it significantly suppresses out-of-focus interference artifacts, which frequently appear in holographic images due to dust particles or other imperfections in various surfaces or optical components of the imaging setup. These naturally occurring artifacts are also highlighted in Fig. 2(f,g,n,o) with yellow arrows and cleaned in the corresponding network output images of Fig. 2(d,e,l,m). From the perspective of our trained neural network, this property to suppress out-of-focus interference artifacts stems from the fact that these holographic artifacts fall into the same category as twin-image artifacts due to the spatial defocusing operation, helping the trained network reject such artifacts in the reconstruction process. This is especially important for coherent imaging systems because various unwanted particles and features form holographic fringes on the sensor plane and superimpose on the object's hologram, degrading the perceived image quality after image reconstruction.

In this study, we used the same neural network architecture depicted in Fig. 1 and Supplementary Figs. 1-2 for all object types, and based on this design, we separately trained the convolutional neural network for different types of objects (e.g., breast tissue vs. Pap smear). The neural network was then fixed after the training process to blindly reconstruct the phase and amplitude images of any object of the same type. If a different type of sample (e.g., a blood smear image) was used as an input for a specific network trained on a different sample type (e.g., Pap smear images), reconstruction artifacts would appear, as exemplified in Supplementary Fig. 6. However, this does not pose a limitation because in most imaging experiments, the type of the sample is known, although its microscopic features are unknown and must be revealed with a microscope. This is the case for biomedical imaging and pathology since the samples are prepared (e.g., stained and fixed) with the correct procedures, tailored for the type of the sample. Therefore, the use of an appropriately trained neural network for a given type of sample can be considered well aligned with traditional uses of digital microscopy tools.

We also created and tested a universal neural network that can reconstruct different types of objects after its training, based on the same architecture used in our earlier networks. To handle different object types using a single neural network, we increased the number of feature maps in each convolutional layer from

16 to 32 (see Supplementary Information), which also increased the complexity of the network, leading to increased training times. However, the reconstruction runtime (after the network was fixed) increased marginally from approximately 6.45 sec to 7.85 sec for a field of view of  $1 \text{ mm}^2$  (see Table 2). Table 1 also compares the SSIM index values achieved using this universal network, which performed similarly to the individual object-type-specific networks. A further comparison between the holographic image reconstructions achieved by this universal network and the object-type-specific networks is also provided in Figure 5, confirming the same conclusion as in Table 1.

## Conclusions

In this paper, we demonstrated that a convolutional neural network can perform phase recovery and holographic image reconstruction after training. This deep learning-based technique provides a new framework in holographic image reconstruction by rapidly eliminating twin-image and self-interference related artifacts using only one hologram intensity. Compared to existing holographic phase recovery approaches, this neural network framework is significantly faster to compute and reconstructs improved phase and amplitude images of the objects with less number of measurements.

## Materials and Methods

### Multi-height phase recovery

To generate the ground truth amplitude and phase images used to train the neural network, phase retrieval was achieved by using a multi-height phase recovery method<sup>19,21,22</sup>. For this purpose, the image sensor is shifted in the  $z$  direction away from the sample by  $\sim 15 \text{ }\mu\text{m}$  increments 6 times and  $\sim 90 \text{ }\mu\text{m}$  increment once, resulting in 8 different relative  $z$  positions of approximately  $0 \text{ }\mu\text{m}$ ,  $15 \text{ }\mu\text{m}$ ,  $30 \text{ }\mu\text{m}$ ,  $45 \text{ }\mu\text{m}$ ,  $60 \text{ }\mu\text{m}$ ,  $75 \text{ }\mu\text{m}$ ,  $90 \text{ }\mu\text{m}$  and  $180 \text{ }\mu\text{m}$ . We refer to these positions as the 1st, 2nd, ..., 8th heights, respectively. The holograms at the 1st, 7th and 8th heights are used to initially calculate the optical phase at the 7th height, using the transport of intensity equation (TIE) through an elliptic equation solver<sup>52</sup> implemented in MATLAB (Release R2016b, The MathWorks, Inc., Natick, Massachusetts). Combined with the square root of the hologram intensity acquired at the 7th height, the resulting complex field is used as an initial guess for the subsequent iterations of the multi-height phase recovery. This initial guess is digitally refocused to the 8th height, where the amplitude of the guess is averaged with the square root of the hologram intensity acquired at the 8th height, and the phase information is kept unchanged. This updating procedure is repeated at the 7th, 6th, ..., 1st heights, which defines one iteration of the algorithm. Usually, 10-20 iterations give satisfactory reconstruction results. However, to ensure the optimality of the phase retrieval for the training of the network, the algorithm is iterated 50 times, after which the complex field is back-propagated to the sample plane, yielding the amplitude and phase or real and imaginary images of the sample. These resulting complex-valued images are used to train the network and provide comparison images for the blind testing of the network output.

### Generation of training data

To generate the training data for the deep neural network, each resulting complex-valued object image

from the multi-height phase recovery algorithm, as well as the corresponding single hologram back-propagation image (which includes the twin-image and self-interference-related spatial artifacts), is divided into  $5 \times 5$  sub-tiles with an overlap of 400 pixels in each dimension. For each sample type, this results in a dataset of 150 image pairs (i.e., complex-valued input images for the network and the corresponding multi-height reconstruction images), which are divided into 100 image pairs for training, 25 image pairs for validation, and 25 image pairs for blind testing. The average computation time for the training of each sample-type-specific deep neural network (which is done only once) was approximately 14.5 hours, whereas it increased to approximately 22 hours for the universal deep neural network (refer to Supplementary Information for additional details). As an example, the progression of the universal network training as a function of the number of epochs is shown in Supplementary Fig. 4.

### **Speeding up holographic image reconstruction using GPU programming**

As further detailed in the Supplementary Information, the pixel super-resolution and multi-height phase retrieval algorithms are implemented in C/C++ and accelerated using the CUDA Application Program Interface (API). These algorithms are run on a laptop computer using a single NVIDIA (Santa Clara, California) GTX 1080 graphics card. The basic image operations are implemented using customized kernel functions and are tuned to optimize the GPU memory access based on the access patterns of individual operations. GPU-accelerated libraries, such as cuFFT<sup>58</sup> and Thrust<sup>59</sup>, are utilized for development productivity and optimized performance. The TIE initial guess is generated using a MATLAB-based implementation, which is interfaced using the MATLAB C++ engine API, allowing the overall algorithm to be maintained within a single executable after compilation.

### **Sample preparation**

*Breast tissue slide:* Formalin-fixed paraffin-embedded (FFPE) breast tissue is sectioned into 2  $\mu\text{m}$  slices and stained using hematoxylin and eosin (H&E). The de-identified and existing slides are obtained from the Translational Pathology Core Laboratory at UCLA.

*Pap smear:* De-identified and existing Papanicolaou smear slides were obtained from the UCLA Department of Pathology.

*Blood smear:* De-identified blood smear slides are purchased from Carolina Biological (Item # 313158).

**References**

- 1 Gerchberg RW, Saxton WO. A practical algorithm for the determination of phase from image and diffraction plane pictures. *Optik* 1972; **35**: 237.
- 2 Fienup JR. Reconstruction of an object from the modulus of its Fourier transform. *Opt Lett* 1978; **3**: 27-29.
- 3 Zalevsky Z, Mendlovic D, Dorsch RG. Gerchberg–Saxton algorithm applied in the fractional Fourier or the Fresnel domain. *Opt Lett* 1996; **21**: 842-844.
- 4 Elser V. Solution of the crystallographic phase problem by iterated projections. *Acta Crystallogr A* 2003; **59**: 201-209.
- 5 Luke DR. Relaxed averaged alternating reflections for diffraction imaging. *Inverse Probl* 2005; **21**: 37-50.
- 6 Latychevskaia T, Fink HW. Solution to the Twin Image Problem in Holography. *Phys Rev Lett* 2007; **98**: 233901.
- 7 Marchesini S. Invited Article: A unified evaluation of iterative projection algorithms for phase retrieval. *Rev Sci Instrum* 2007; **78**: 011301.
- 8 Quiney HM, Williams GJ, Nugent KA. Non-iterative solution of the phase retrieval problem using a single diffraction measurement. *Opt Express* 2008; **16**: 6896-6903.
- 9 Brady DJ, Choi K, Marks DL, Horisaki R, Lim S. Compressive holography. *Opt Express* 2009; **17**: 13040-13049.
- 10 Szameit A, Shechtman Y, Osherovich E, Bullkich E, Sidorenko P *et al.* Sparsity-based single-shot subwavelength coherent diffractive imaging. *Nat Mater* 2012; **11**: 455-459.
- 11 Candès EJ, Eldar YC, Strohmer T, Voroninski V. Phase retrieval via matrix completion. *SIAM J Imaging Sci* 2013; **6**: 199-225.
- 12 Rodriguez JA, Xu R, Chen CC, Zou YF, Miao JW. Oversampling smoothness: an effective algorithm for phase retrieval of noisy diffraction intensities. *J Appl Crystallogr* 2013; **46**: 312-318.

- 13 Rivenson Y, Aviv (Shalev) M, Weiss A, Panet H, Zalevsky Z. Digital resampling diversity sparsity constrained-wavefield reconstruction using single-magnitude image. *Opt Lett* 2015; **40**: 1842-1845.
- 14 Gabor D. A new microscopic principle. *Nature* 1948; **161**: 777-778.
- 15 Faulkner HML, Rodenburg JM. Movable aperture lensless transmission microscopy: a novel phase retrieval algorithm. *Phys Rev Lett* 2004; **93**: 023903.
- 16 Dierolf M, Menzel A, Thibault P, Schneider P, Kewish CM *et al.* Ptychographic X-ray computed tomography at the nanoscale. *Nature* 2010; **467**: 436-439.
- 17 Zheng GA, Horstmeyer R, Yang C. Wide-field, high-resolution Fourier ptychographic microscopy. *Nat Photonics* 2013; **7**: 739-745.
- 18 Tian L, Waller L. 3D intensity and phase imaging from light field measurements in an LED array microscope. *Optica* 2015; **2**: 104-111.
- 19 Misell DL. An examination of an iterative method for the solution of the phase problem in optics and electron optics: I. Test calculations. *J Phys D Appl Phys* 1973; **6**: 2200-2216.
- 20 Teague MR. Deterministic phase retrieval: a Green's function solution. *J Opt Soc Am* 1983; **73**: 1434-1441.
- 21 Paganin D, Barty A, McMahon PJ, Nugent KA. Quantitative phase-amplitude microscopy. III. The effects of noise. *J Microsc* 2004; **214**: 51-61.
- 22 Greenbaum A, Ozcan A. Maskless imaging of dense samples using pixel super-resolution based multi-height lensfree on-chip microscopy. *Opt Express* 2012; **20**: 3129-3143.
23. Rivenson Y, Wu Y, Wang H, Zhang Y, Feizi A *et al.* Sparsity-based multi-height phase recovery in holographic microscopy. *Sci Rep* 2016; **6**: 37862
24. Wang H, Göröcs Z, Luo W, Zhang Y, Rivenson Y. *et al.* Computational out-of-focus imaging increases the space–bandwidth product in lensbased coherent microscopy. *Optica* 2016; **3**: 1422–1429 .

- 25 Ferraro P, Miccio L, Grilli S, Paturzo M, De Nicola S *et al.* Quantitative Phase Microscopy of microstructures with extended measurement range and correction of chromatic aberrations by multiwavelength digital holography. *Opt Express* 2007; **15**: 14591-14600.
- 26 Luo W, Zhang YB, Feizi A, Göröcs Z, Ozcan A. Pixel super-resolution using wavelength scanning. *Light Sci Appl* 2016; **5**: e16060.
- 27 Gonsalves RA. Phase retrieval and diversity in adaptive optics. *Opt Eng* 1982; **21**: 215829.
- 28 Eisebitt S, Lüning J, Schlotter WF, Lörngen M, Hellwig O *et al.* Lensless imaging of magnetic nanostructures by X-ray spectro-holography. *Nature* 2004; **432**: 885-888.
- 29 Rosen J, Brooker G. Non-scanning motionless fluorescence three-dimensional holographic microscopy. *Nat Photonics* 2008; **2**: 190-195.
- 30 Marchesini S, Boutet S, Sakdinawat AE, Bogan MJ, Bajt S *et al.* Massively parallel X-ray holography. *Nat Photonics* 2008; **2**: 560-563.
- 31 Popescu G, Ikeda T, Dasari RR, Feld MS. Diffraction phase microscopy for quantifying cell structure and dynamics. *Opt Lett* 2006; **31**: 775-777.
- 32 Coppola G, Di Caprio G, Gioffré M, Puglisi R, Balduzzi D *et al.* Digital self-referencing quantitative phase microscopy by wavefront folding in holographic image reconstruction. *Opt Lett* 2010; **35**: 3390-3392.
- 33 Wang Z, Millet L, Mir M, Ding HF, Unarunotai S *et al.* Spatial light interference microscopy (SLIM). *Opt Express* 2011; **19**: 1016-1026.
- 34 Rivenson Y, Katz B, Kelner R, Rosen J. Single channel in-line multimodal digital holography. *Opt Lett* 2013; **38**: 4719-4722.
- 35 Shechtman Y, Eldar YC, Cohen O, Chapman HN, Miao JW *et al.* Phase retrieval with application to optical imaging: a contemporary overview. *IEEE Signal Process Mag* 2015; **32**: 87-109.
- 36 Kelner R, Rosen J. Methods of single-channel digital holography for three-dimensional imaging. *IEEE Trans Ind Inform* 2016; **12**: 2201-1230; doi: 10.1109/TII.2015.2475247.

- 37 Zuo JM, Vartanyants I, Gao M, Zhang R, Nagahara LA. Atomic resolution imaging of a carbon nanotube from diffraction intensities. *Science* 2003; **300**: 1419-1421.
- 38 Song CY, Jiang HD, Mancuso A, Amirbekian B, Peng L *et al.* Quantitative imaging of single, unstained viruses with coherent X rays. *Phys Rev Lett* 2008; **101**: 158101.
- 39 Miao JW, Ishikawa T, Shen Q, Earnest T. Extending X-ray crystallography to allow the imaging of noncrystalline materials, cells, and single protein complexes. *Annu Rev Phys Chem* 2008; **59**: 387-410.
- 40 Loh ND, Hampton CY, Martin AV, Starodub D, Sierra RG *et al.* Fractal morphology, imaging and mass spectrometry of single aerosol particles in flight. *Nature* 2012; **486**: 513-517.
- 41 LeCun Y, Bengio Y, Hinton G. Deep learning. *Nature* 2015; **521**: 436-444.
- 42 Schmidhuber J. Deep learning in neural networks: An overview. *Neural Netw* 2015; **61**: 85-117.
- 43 Dong C, Loy CC, He KM, Tang XO. Image super-resolution using deep convolutional networks. *IEEE Trans Pattern Anal Mach Intell* 2016; **38**: 295-307.
- 44 Rivenson Y, Gorocs Z, Gunaydin H, Zhang YB, Wang HD *et al.* Deep learning microscopy. arXiv: 1705.04709, 2017.
- 45 Jin KH, McCann MT, Froustey E, Unser M. Deep convolutional neural network for inverse problems in imaging. *IEEE Trans Image Process* 2017; **26**: 4509-4522.
- 46 Wang SS, Su ZH, Ying L, Peng X, Zhu S *et al.* Accelerating magnetic resonance imaging via deep learning. Proceedings of the 13th International Symposium on Biomedical Imaging (ISBI); 13-16 April 2016; Prague, Czech Republic. IEEE: Prague, Czech Republic, 2016; doi: 10.1109/ISBI.2016.7493320.
- 47 Antholzer S, Haltmeier M, Schwab J. Deep learning for photoacoustic tomography from sparse data. arXiv:1704.04587, 2017.
- 48 Jo Y, Park S, Jung J, Yoon J, Joo H *et al.* Holographic deep learning for rapid optical screening of anthrax spores. *Sci Adv* 2017; **3**: e1700606.

- 49 Sinha A, Lee J, Li S, Barbastathis G. Lensless computational imaging through deep learning. arXiv: 1702.08516, 2017.
- 50 Bartels M, Krenkel M, Haber J, Wilke RN, Salditt T. X-ray holographic imaging of hydrated biological cells in solution. *Phys Rev Lett* 2015; **114**: 048103.
- 51 McNulty I, Kirz J, Jacobsen C, Anderson EH, Howells MR *et al.* High-resolution imaging by Fourier transform X-ray holography. *Science* 1992; **256**: 1009-1012.
- 52 Greenbaum A, Zhang YB, Feizi A, Chung PL, Luo W *et al.* Wide-field computational imaging of pathology slides using lens-free on-chip microscopy. *Sci Transl Med* 2014; **6**: 267ra175-267.
- 53 Nowlan SJ, Hinton GE. Simplifying neural networks by soft weight-sharing. *Neural Comput* 1992; **4**: 473-493.
- 54 Wang Z, Bovik AC, Sheikh HR, Simoncelli EP. Image Quality Assessment: From Error Visibility to Structural Similarity. *IEEE Trans Image Process* 2004; **13**: 600-612.
- 55 Lohmann A. Optische einseitenbandübertragung angewandt auf das Gabor-Mikroskop. *Opt Acta* 1956; **3**: 97-99.
- 56 Leith EN, Upatnieks J. Reconstructed wavefronts and communication theory. *J Opt Soc Am* 1962; **52**: 1123-1130.
- 57 Goodman JW. *Introduction to Fourier Optics*. 3rd edn. Greenwood Village, Colorado: Roberts and Company Publishers; 2005.
- 58 cuFFT. *NVIDIA Developer* (2012). Available at: <https://developer.nvidia.com/cufft>. (Accessed: 9th April 2017) (The content in the link is not NVIDIA Developer)
- 59 Thrust-Parallel Algorithms Library. Available at: <https://thrust.github.io/>. (Accessed: 9th April 2017) (The content in the link is not NVIDIA Developer)

Accepted Manuscript

## Figures and Tables

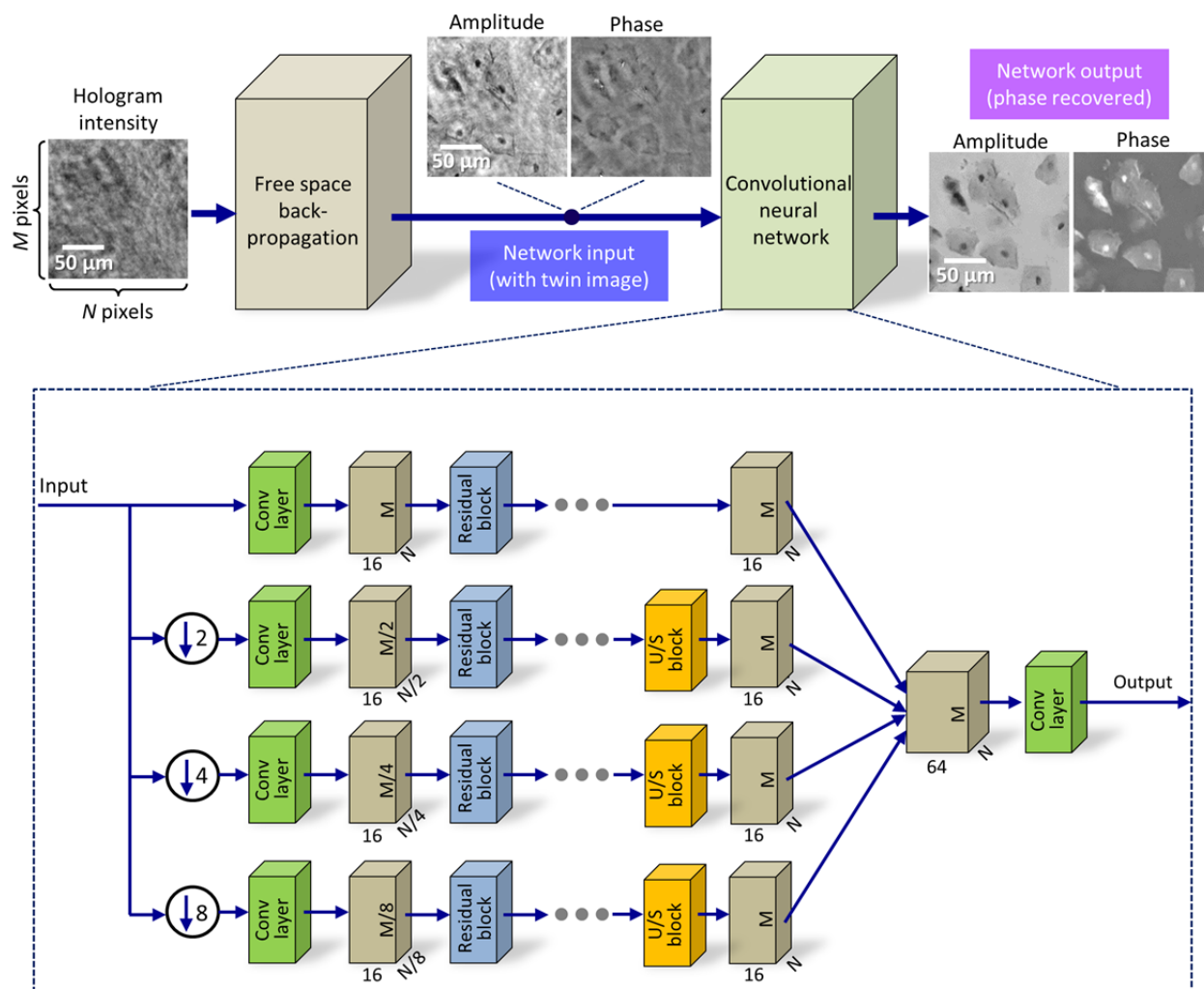


**Fig. 1.** Following its training phase, the deep neural network blindly outputs artifact-free phase and amplitude images of the object using only one hologram intensity. This deep neural network is composed of convolutional layers, residual blocks and upsampling blocks (see Supplementary Information for additional details) and rapidly processes a complex-valued input image in a parallel, multi-scale manner.

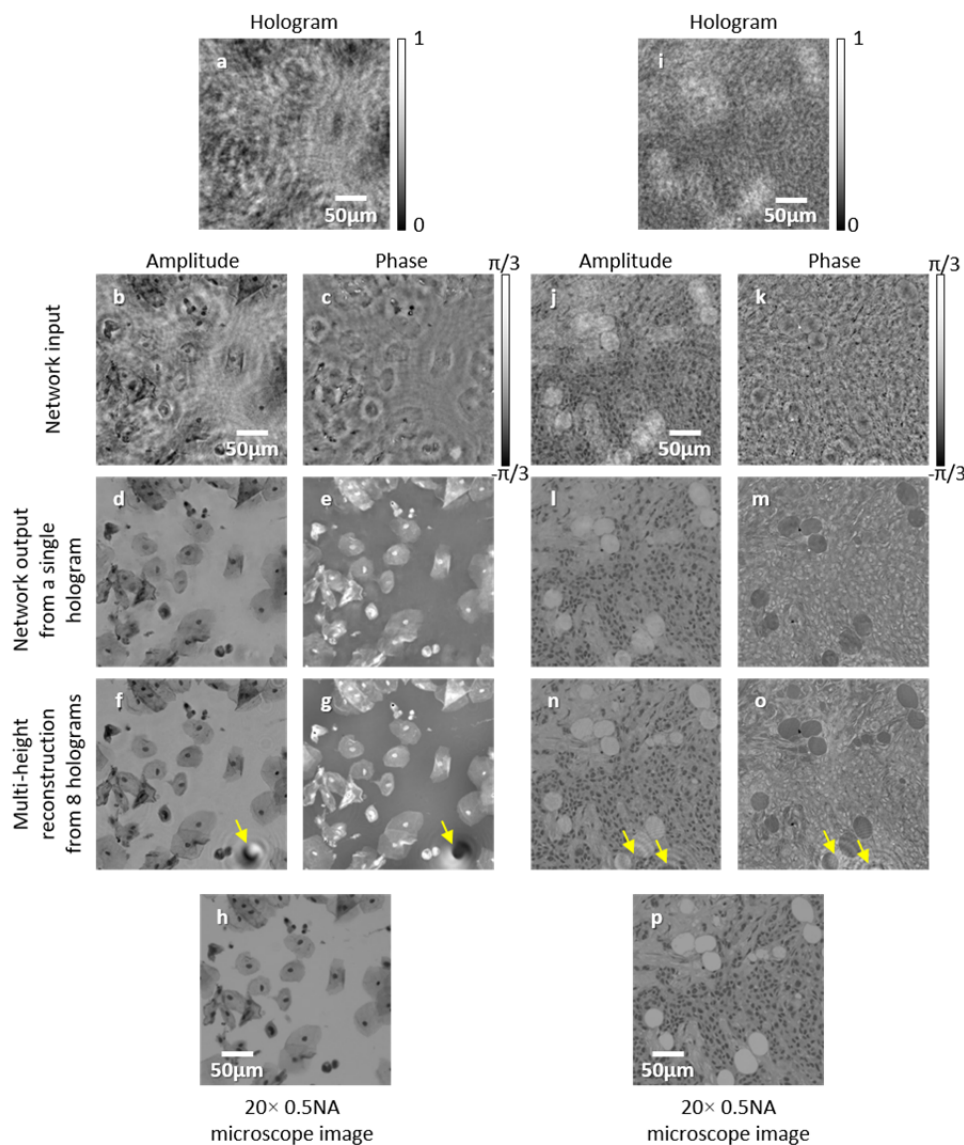


**Fig. 2.** Comparison of the holographic reconstruction results for different types of samples: **(a-h)** Pap smear, **(i-p)** breast tissue section. **a, i**, zoomed-in regions of interest from the acquired holograms. **b, c, j, k** amplitude and phase images resulting from free-space back-propagation of a single hologram intensity, shown in **a** and **i**, respectively. These images are contaminated with twin-image and self-interference-related spatial artifacts due to the missing phase information in the hologram detection process. **d, e, l, m**, corresponding amplitude and phase images of the same samples obtained by the deep neural network, demonstrating the blind recovery of the complex object image without twin-image and self-interference artifacts using a single hologram. **f, g, n, o**, amplitude and phase images of the same samples reconstructed using multi-height phase retrieval with 8 holograms acquired at different sample-to-sensor distances. **h, p**, corresponding bright-field microscopy images of the same samples, shown for comparison. The yellow arrows point to artifacts in **f, g, n, o** (due to out-of-focus dust particles or other unwanted objects) that are significantly suppressed by the network reconstruction, as shown in **d, e, l, m**.

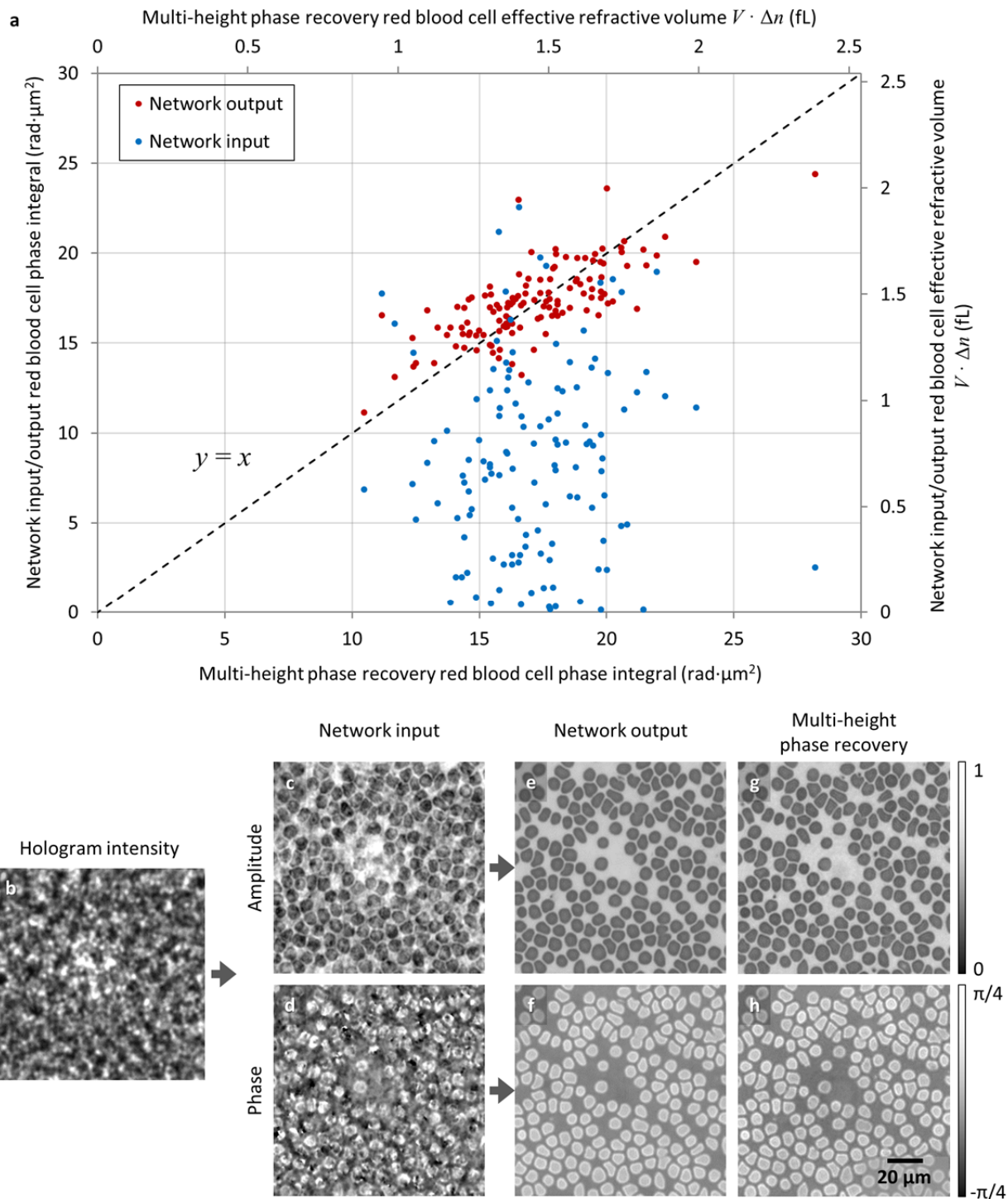


**Fig. 3.** Red blood cell volume estimation using our deep neural network-based phase retrieval. The deep neural network output (**e, f**), given the input (**c, d**) obtained from a single hologram intensity (**b**), shows a good match with the multi-height phase recovery-based cell volume estimation results (**a**), calculated using  $N_{\text{holo}} = 8$  (**g, h**). Similar to the yellow arrows shown in Fig. 2(**f, g, n, o**), the multi-height phase recovery results exhibit an out-of-focus fringe artifact at the center of the field-of-view in (**g, h**). Refer to Supplementary Information for the calculation of the effective refractive volume of cells.

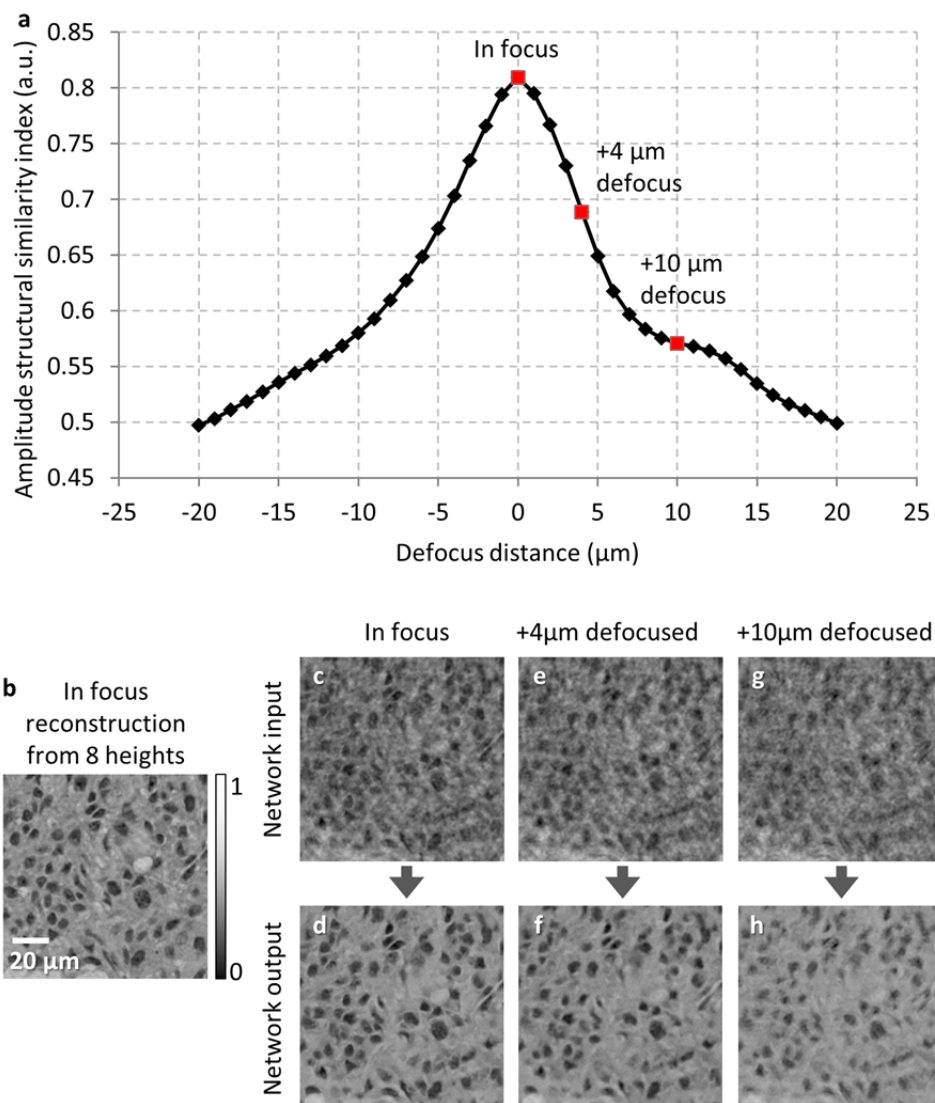


**Fig. 4.** Estimation of the depth defocusing tolerance of the deep neural network. **a**, SSIM index for the neural network output images when the input image is defocused (i.e., deviates from the optimal focus used in the training of the network). The SSIM index compares the network output images in **d**, **f**, **h**, with the image obtained by using the multi-height phase recovery algorithm with  $N_{\text{holo}} = 8$ , shown in **b**.

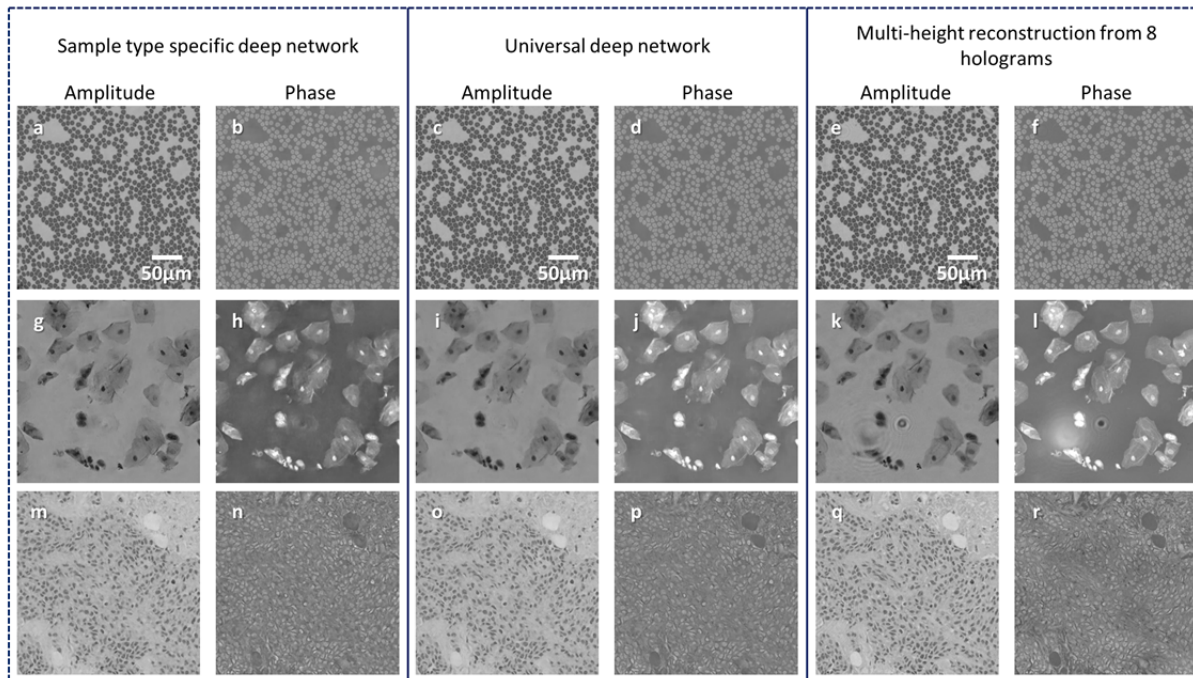


**Fig. 5.** Comparison of the holographic image reconstruction results for the sample-type-specific and universal deep networks for different types of samples. The deep neural network used a single hologram intensity as input, whereas  $N_{\text{holo}} = 8$  was used in the column on the right. **(a-f)** Blood smear. **(g-l)** Papanicolaou smear. **(m-r)** Breast tissue section.

Reconstruction method \ Sample type	Deep network input ( $N_{\text{holo}}=1$ )	Deep network output (Sample type specific) ( $N_{\text{holo}}=1$ )	Deep network output (Universal) ( $N_{\text{holo}}=1$ )	Multi-height phase-recovery ( $N_{\text{holo}}=2$ )	Multi-height phase-recovery ( $N_{\text{holo}}=3$ )	Multi-height phase-recovery ( $N_{\text{holo}}=4$ )	Multi-height phase-recovery ( $N_{\text{holo}}=5$ )	Multi-height phase-recovery ( $N_{\text{holo}}=6$ )	Multi-height phase-recovery ( $N_{\text{holo}}=7$ )	Multi-height phase-recovery ( $N_{\text{holo}}=8$ )
Pap smear <i>real part</i>	0.726	<b>0.895</b>	<b>0.893</b>	0.875	0.922	0.954	0.979	0.985	0.986	1
Pap smear <i>imaginary part</i>	0.431	<b>0.870</b>	<b>0.870</b>	0.840	0.900	0.948	0.979	0.986	0.987	1
Blood smear <i>real part</i>	0.701	<b>0.942</b>	<b>0.951</b>	0.890	0.942	0.962	0.970	0.975	0.977	1
Blood smear <i>imaginary part</i>	0.048	<b>0.930</b>	<b>0.925</b>	0.46	0.849	0.907	0.935	0.938	0.955	1
Breast tissue <i>real part</i>	0.826	<b>0.916</b>	<b>0.921</b>	0.931	0.955	0.975	0.981	0.983	0.984	1
Breast tissue <i>imaginary part</i>	0.428	<b>0.912</b>	<b>0.916</b>	0.911	0.943	0.970	0.979	0.981	0.982	1

**Table 1.** Comparison of the SSIM index values between the deep neural network output images obtained with a single hologram intensity (for both the sample-type-specific and universal networks) and the multi-height phase retrieval results for different numbers of input holograms ( $N_{\text{holo}}$ ) corresponding to Pap smear samples, breast tissue histopathology slides and blood smear samples. In each case, the SSIM index is separately calculated for the *real* and *imaginary* parts of the resulting complex-valued image with respect to the multi-height phase recovery result for  $N_{\text{holo}}=8$ , and thus, by definition, the last column on the right has an SSIM index of 1. Due to the presence of twin-image and self-interference artifacts, the first column formed by the input images has the worst performance.

	Deep network output (Sample type specific)	Deep network output (Universal)	Multi-height phase-recovery						
	( $N_{\text{holo}}=1$ )	( $N_{\text{holo}}=1$ )	( $N_{\text{holo}}=2$ )	( $N_{\text{holo}}=3$ )	( $N_{\text{holo}}=4$ )	( $N_{\text{holo}}=5$ )	( $N_{\text{holo}}=6$ )	( $N_{\text{holo}}=7$ )	( $N_{\text{holo}}=8$ )
Runtime (sec)	6.45	7.85	23.20	28.32	32.11	35.89	38.28	43.13	47.43

**Table 2.** Comparison of the holographic image reconstruction runtime for a field of view of  $\sim 1 \text{ mm}^2$  for different phase recovery approaches. All the reconstructions were performed on a laptop using a single GPU (see Supplementary Information for details). Of the 6.45 sec and 7.85 sec required for image reconstruction from a single hologram intensity using sample-type-specific and universal neural networks, respectively, the deep neural network processing time is 3.11 sec for the sample-type-specific network and 4.51 sec for the universal network, while the rest of the time (i.e., 3.34 sec for the preprocessing stages) is used for other operations such as pixel super-resolution, auto-focusing and free space back-propagation.

## Supplementary Information

### Phase recovery and holographic image reconstruction using deep learning in neural networks

Yair Rivenson<sup>1,2,3,†</sup>, Yibo Zhang<sup>1,2,3,†</sup>, Harun Günaydin<sup>1</sup>, Da Teng<sup>1,4</sup>, Aydogan Ozcan<sup>1,2,3,5,\*</sup>

<sup>1</sup>*Electrical Engineering Department, University of California, Los Angeles, CA, 90095, USA.*

<sup>2</sup>*Bioengineering Department, University of California, Los Angeles, CA, 90095, USA.*

<sup>3</sup>*California NanoSystems Institute (CNSI), University of California, Los Angeles, CA, 90095, USA.*

<sup>4</sup>*Computer Science Department, University of California, Los Angeles, CA, 90095, USA*

<sup>5</sup>*Department of Surgery, David Geffen School of Medicine, University of California, Los Angeles, CA, 90095, USA.*

\*Correspondence: [ozcan@ucla.edu](mailto:ozcan@ucla.edu)

## Network architecture

Our deep neural network architecture is detailed in Fig. 1 and Supplementary Figs. 1-2. The real and imaginary parts of the back-propagated hologram intensity are used as two input image channels to the network, each with a size of  $M \times N$  pixels (e.g.,  $M = 1392$ ,  $N = 1392$ ). Although not considered here, in an alternative implementation a different network design could possibly use the raw hologram intensity as input, without a wave back-propagation step. These two channels (real and imaginary parts) of the network are then used *simultaneously* as input to 4 convolutional layers. The output of each convolutional layer is 16 channels (feature maps), each with a size of  $M \times N$  pixels, which was empirically determined to balance the deep network size/compactness and performance. The value of  $x, y$ -th pixel in the  $j$ -th feature map in the  $i$ -th convolutional layer is given by  $v_{i,j}^{x,y}$ :<sup>1</sup>

$$v_{i,j}^{x,y} = \sum_r \sum_{p=0}^{P-1} \sum_{q=0}^{Q-1} w_{i,j,r}^{p,q} v_{i-1,r}^{x+p,y+q} + b_{i,j} \quad (s1)$$

where  $b_{i,j}$  is a common bias term for the  $j$ -th feature map,  $r$  indicates the set of the feature maps in the  $i-1$  layer (which is 2, for the first convolutional layer),  $w_{i,j,r}^{p,q}$  is the value of the convolution kernel at the  $p, q$ -th position,  $P$  and  $Q$  define the size of the convolutional kernels, which is  $3 \times 3$  throughout the network in our implementation.

For object type-based deep networks, the output of these 4 convolutional layers is then downsampled by  $\times 1$ ,  $\times 2$ ,  $\times 4$ ,  $\times 8$ , creating 4 different data flow paths, with 16 channels and spatial dimensions of  $M \times N$ ,  $M/2 \times N/2$ ,  $M/4 \times N/4$  and  $M/8 \times N/8$ , respectively. This multi-scale data processing scheme was created to allow the network to learn how to suppress the twin-image and self-interference artifacts, created by objects with different feature sizes. The output of these downsampling operators is followed by 4 residual blocks<sup>2</sup>, each composed of 2 convolutional layers and 2 activation functions, which we chose to implement as rectified linear units (ReLU), i.e.,  $\text{ReLU}(x) = \max(0, x)$ . Residual blocks create a shortcut between the block's input and output, which allows a clear path for information flow between layers<sup>3</sup>. This has been demonstrated to speed up the convergence of the training phase of the deep neural network. While some of the previously reported residual block architectures contain batch normalization layers, we observed that the addition of such layers into our network reduces the inference performance and the quality of the phase retrieval results, and therefore we did not use batch normalization in our architecture. Following the 4 residual blocks, data at each scale are upsampled to match the original data dimensions. Each upsampling block<sup>4</sup> (i.e., U/S block in Supplementary Fig. 1) contains a convolutional layer that takes 16 channels, each with  $M/L \times N/L$  pixels as input, and outputs 64 channels each with  $M/L \times N/L$  pixels ( $L=2, 4, 8$ ). This is followed by a ReLU operation and an upsampling layer, which is schematically detailed in Supplementary Fig. 2. This layer learns to upsample a 64 channel input (each with  $M/L \times N/L$  pixels) to a 16 channel output (each with  $2M/L \times 2N/L$  pixels). This upsampling process is being performed once, twice, or three times, for the  $\times 2$ ,  $\times 4$ ,  $\times 8$  spatially downsampled network inputs, respectively (see Supplementary Fig. 1). The output of each one of these 4 different dataflow paths (with 16 channels,  $M \times N$  pixels, following the upsampling stage) is concatenated to a 64 channels input, which results in 2 channels: one for the real part and one for the imaginary part of the object image, each having  $M \times N$  pixels. For the universal deep network, we kept the same architecture;

however, we increased the number of channels in the output of each convolutional layer by two-fold, i.e., from 16 to 32 in the residual blocks.

To train the network, we minimized the average of the mean-squared-errors of the real and imaginary parts of the network output with respect to the real and imaginary parts of the object’s ground truth images, obtained using multi-height phase retrieval with 8 holograms recorded at different sample-to-sensor distances (also see the Methods section of the main text). This loss function over a mini-batch of  $K$  input patches (images) is calculated as:

$$Loss(\Theta) = \frac{1}{2K} \sum_{k=1}^K \left\{ \frac{1}{M \times N} \sum_{m=1}^M \sum_{n=1}^N \|Y_{Re,m,n,k}^{\Theta} - Y_{Re,m,n,k}^{GT}\|^2 + \frac{1}{M \times N} \sum_{m=1}^M \sum_{n=1}^N \|Y_{Im,m,n,k}^{\Theta} - Y_{Im,m,n,k}^{GT}\|^2 \right\} \quad (s2)$$

where  $k$  is the  $k$ -th image patch,  $Y_{Re,m,n,k}^{\Theta}$ ,  $Y_{Im,m,n,k}^{\Theta}$  denote the  $m,n$ -th pixel of real and imaginary network outputs, respectively, and  $Y_{Re,m,n,k}^{GT}$ ,  $Y_{Im,m,n,k}^{GT}$  denote the  $m,n$ -th pixel of real and imaginary parts of the training (i.e., ground truth) labels, respectively. The network’s parameter space (e.g., kernels, biases, weights) is defined by  $\Theta$  and its output is given by

$[Y_{Re}^{\Theta}, Y_{Im}^{\Theta}] = F(X_{Re,input}, X_{Im,input}; \Theta)$ , where  $F$  defines the deep neural network’s operator on the back propagated complex field generated from a single hologram intensity, divided into real and imaginary channels,  $X_{Re,input}$ ,  $X_{Im,input}$ , respectively. Following the estimation of the loss function, the resulting error in the network output is back-propagated through the network and the Adaptive Moment Estimation<sup>5</sup> (ADAM) based optimization is used to tune the network’s parameter space,  $\Theta$ , with a learning rate of  $10^{-4}$ . For the sample type specific network training, we used a batch size of  $K=2$  and an image size of  $1392 \times 1392$  pixels. For the universal deep network, we divided the image dataset to  $256 \times 256$ -pixel patches (with an overlap of 20% between the patches) and a mini-batch size of  $K=30$  (see Supplementary Fig. 3). For both the sample type specific and universal networks, the images that we used to test the network had a size of  $1392 \times 1392$  pixels. All the convolutional kernel entries are initialized using a truncated normal distribution. All the network bias terms,  $b_{i,j}$ , are initialized to 0. In case the size of the input image is not divisible by 8, zero padding is performed on it such that it becomes divisible by 8.

As an example, the progression of the universal deep network training is shown Supplementary Fig. 4 by plotting the training and validation dataset errors as a function of the number of training epochs (i.e., the number of passes on the entire dataset with backpropagation through the network).

### Network implementation details

For our programming, we used Python version 3.5.2, and the deep neural network was implemented using TensorFlow framework version 1.1.0 (Google). We used a laptop computer with Core i7-6700K CPU @ 4GHz (Intel) and 64GB of RAM, running a Windows 10 operating system (Microsoft). The network training was performed using GeForce GTX 1080 (Nvidia) Dual Graphical Processing Units (GPUs). The testing of the network was performed on *a single GPU* to provide a fair comparison against multi-height phase retrieval CUDA implementation, as summarized in Table 2 (main text).

## Optical set-up

Our experimental set-up (Supplementary Fig. 5) includes a laser source (SC400, Fianium Ltd., Southampton, UK) filtered by an acousto-optic tunable filter and coupled to a single mode optical fiber to provide partially coherent illumination with a spectral bandwidth of  $\sim 2.5$  nm. A CMOS image sensor with  $1.12 \mu\text{m}$  pixel size and 16.4 Megapixel (IMX081, Sony Corp., Japan) is used to capture the holographic images. The distance from the optical fiber tip to the sample is between 7 and 15 cm, such that the light that is incident on the sample can be considered a quasi-plane wave. The distance from the sample to the image sensor plane is approximately  $300\text{-}700 \mu\text{m}$ . This unit magnification geometry results in a large field of view that is equal to the image sensor's active area. The image sensor was mounted on a 3D positioning stage (NanoMax 606, Thorlabs Inc., New Jersey, US), which moved it in  $x$  and  $y$  directions in sub-pixel-size steps to implement pixel super-resolution (PSR). The image sensor was also shifted in the  $z$  direction with step sizes of a few tens of microns to perform multi-height phase recovery to generate training data for the neural network. A custom-written LabVIEW program implemented on a desktop computer was used to control and automate all of these components as part of the imaging set-up.

## Pixel super resolution (PSR)

In order to mitigate the spatial undersampling caused by the relatively large pixel pitch of the image sensor chip ( $\sim 1.12 \mu\text{m}$ ), multiple subpixel-shifted holograms were used to synthesize a higher resolution (i.e., pixel super-resolved) hologram. For this, the image sensor was mechanically shifted by a 6-by-6 rectangular grid pattern in the  $x$ - $y$  plane, with increments of  $0.37 \mu\text{m}$ , corresponding to approximately  $1/3$  of the image sensor's pixel size. A 6-by-6 grid ensured that one color channel of the Bayer pattern could cover its entire period. In an alternative design with a monochrome image sensor (instead of an RGB sensor), only a 3-by-3 grid would be needed to achieve the same PSR factor. For this PSR computation, an efficient non-iterative fusion algorithm was applied to combine these sub-pixel shifted images into one higher-resolution hologram, which preserves the optimality of the solution in the maximum likelihood sense<sup>6</sup>. The selection of which color channel (R, G or B) of the Bayer pattern to use for holographic imaging is based on pixel sensitivity to the illumination wavelength that is used. For example, at  $\sim 530$  nm illumination, the two green channels of the Bayer pattern were used, and at  $\sim 630$  nm, the red channel was used.

## Calculation of red blood cell (RBC) phase integral and effective refractive volume

The relative optical phase delay due to a cell, with respect to the background, can be approximated as:

$$\varphi(x, y) = \frac{2\pi d(x, y) \cdot \Delta n(x, y)}{\lambda} \quad (\text{s3})$$

where  $d(x, y)$  is the thickness of the sample (e.g., an RBC) as a function of the lateral position,  $\Delta n(x, y) = n(x, y) - n_0$  is the refractive index difference between the sample ( $n(x, y)$ ) and the background medium ( $n_0$ ),  $\lambda$  is the illumination wavelength in air. Based on these, we define the phase integral for a given RBC image as:

$$p_i = \left| \int_{S_i} \varphi(x, y) ds \right| = \left| \int_{S_i} \frac{2\pi d(x, y) \Delta n(x, y)}{\lambda} ds \right| \quad (\text{s4})$$

which calculates the relative phase with respect to the background that is integrated over the area of each RBC (defined by  $S_i$ ), which results in a unit of  $\text{rad} \cdot \mu\text{m}^2$ . Let  $\Delta n$  represent the average refractive index difference within each cell (with respect to  $n_0$ ), we can then write:

$$p_i = \frac{2\pi \cdot |\Delta n|}{\lambda} \int_{S_i} d(x, y) \cdot ds = \frac{2\pi \cdot |\Delta n|}{\lambda} \cdot V_i \quad (\text{s5})$$

where  $V_i$  represents the volume of the  $i$ -th cell. Because the average refractive index of a *fixed and stained* RBC (as one would have in a blood smear sample) is hard to determine or estimate, we instead define *effective refractive volume of an RBC* as:

$$\tilde{V}_i = |\Delta n| \cdot V_i = \frac{p_i \lambda}{2\pi} \quad (\text{s6})$$

which also has the unit of volume (e.g., femtoliter, fL).

### Structural similarity (SSIM) index calculation

The structural similarity index between two images  $I_1$  and  $I_2$  can be calculated as<sup>7</sup>:

$$\text{SSIM}(I_1, I_2) = \frac{(2\mu_1\mu_2 + c_1)(2\sigma_{1,2} + c_2)}{(\mu_1^2 + \mu_2^2 + c_1)(\sigma_1^2 + \sigma_2^2 + c_2)} \quad (\text{s7})$$

where  $\mu_1$  is the average of  $I_1$ ,  $\mu_2$  is the average of  $I_2$ ,  $\sigma_1^2$  is the variance of  $I_1$ ,  $\sigma_2^2$  is the variance of  $I_2$ ,  $\sigma_{1,2}$  is the cross-covariance of  $I_1$ , and  $I_2$ . The stabilization constants ( $c_1, c_2$ ) prevent division by a small denominator and can be selected as  $c_1 = (K_1 L)^2$  and  $c_2 = (K_2 L)^2$ , where  $L$  is the dynamic range of the image and  $K_1, K_2$  are both much smaller than 1. SSIM index between two images ranges between 0 and 1 (the latter for identical images).

### Evaluation of scattering strength of the samples

To evaluate the validity of the weakly scattering condition, i.e.,  $|a(x, y)| \ll A$  for the samples that we imaged (see the Discussion section of the main text), we took a region of interest for each of the samples that is reconstructed using the multi-height phase recovery, based on 8 hologram heights. After the phase recovery step, we have:

$$u = A + a(x, y) \quad (\text{s8})$$

where  $A$  can be estimated by calculating the average value of a background region where no sample is present. After  $A$  is estimated, we calculate a normalized complex image  $\tilde{u}$ ,

$$\tilde{u} = \frac{u}{A} = 1 + \frac{a(x,y)}{A} \quad (\text{s9})$$

Next, we define  $R$  as the ratio between the root-mean-squared (RMS, or quadratic mean) modulus of the scattered wave  $|a(x,y)|$  divided by the reference wave modulus  $|A|$ , to obtain:

$$R = \frac{\langle |a(x,y)|^2 \rangle^{1/2}}{|A|} = \langle |\tilde{u} - 1|^2 \rangle^{1/2} \quad (\text{s10})$$

where  $\langle \bullet \rangle$  denotes 2D spatial averaging operation. This ratio,  $R$ , is used to evaluate the validity of the weakly scattering condition for our samples, and is found to be 0.28, 0.34, and 0.37 for the breast tissue, Pap smear and blood smear samples that we imaged, respectively (see the Discussion section).

### Calculation of the sample-to-sensor distance

The relative separation between successive image sensor heights (or hologram planes) needs to be estimated to successfully apply the TIE and multi-height phase recovery algorithms, and the absolute  $z_2$  distance (i.e., the sample-to-sensor distance, see Supplementary Fig. 5) is needed for the final back-propagation of the recovered complex wave onto the sample plane. Estimating the relative  $z$ -separation is done by using an autofocusing algorithm based on an axial magnitude differential metric, i.e.,

$$z_{focus} = \arg \min_z \left[ \frac{\partial}{\partial z} \sum_{x,y} |U_{ROI}(x,y;z)| \right] \quad (\text{s11})$$

where  $U_{ROI}(x,y;z)$  is the propagated complex optical wavefront at a distance of  $z$ , and cropped to a certain region of interest (ROI).

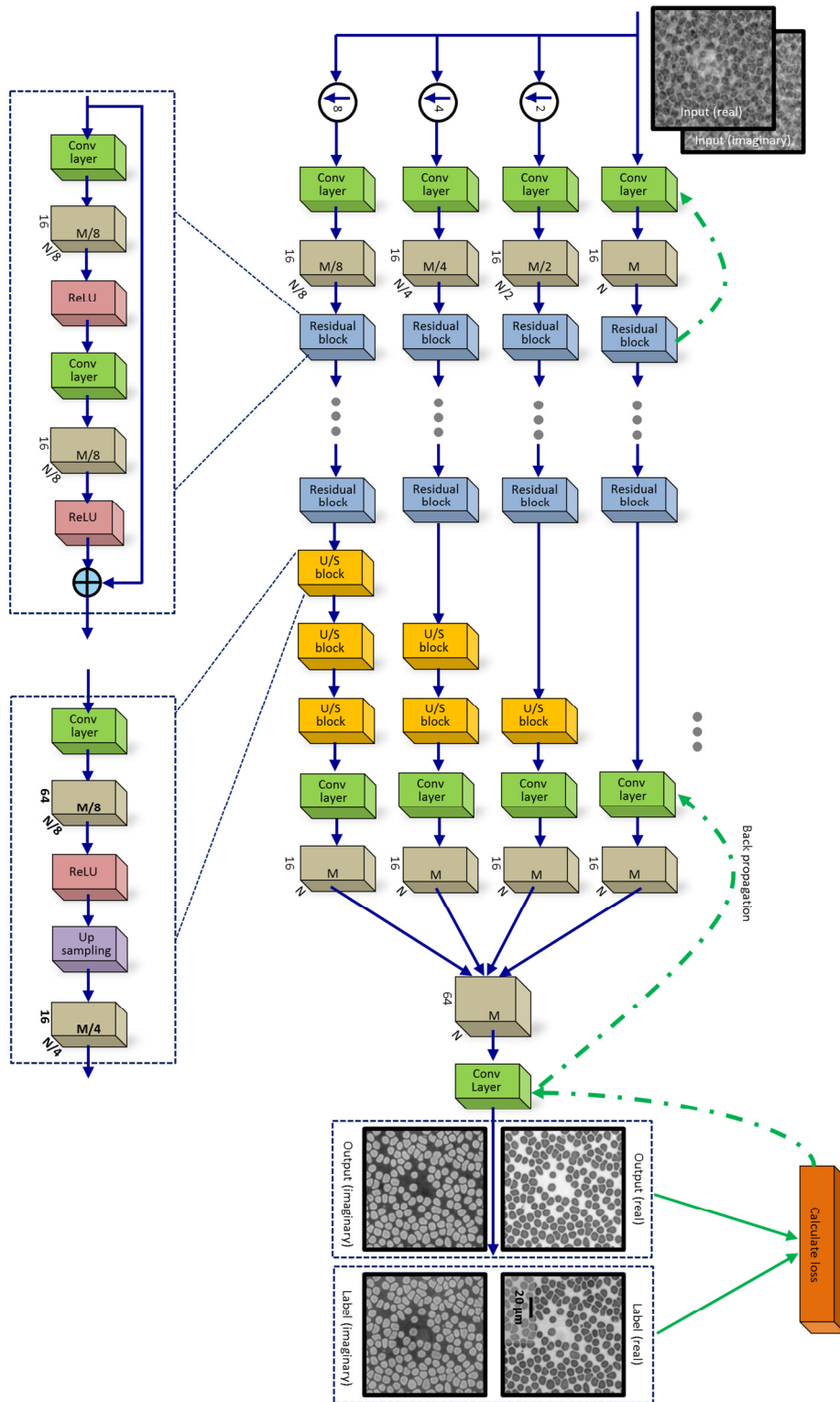
For computational efficiency, first a coarse scan is done between 100  $\mu\text{m}$  and 800  $\mu\text{m}$  with a step size of 10  $\mu\text{m}$ . Then, around the minimum that is found by this coarse scan, a golden section search algorithm<sup>8</sup> is applied to locate the minimum with a final precision of 0.01  $\mu\text{m}$ . The absolute  $z_2$  is refined after the convergence of the multi-height phase recovery algorithm by refocusing the phase-recovered hologram near the previously found focus point.

### References

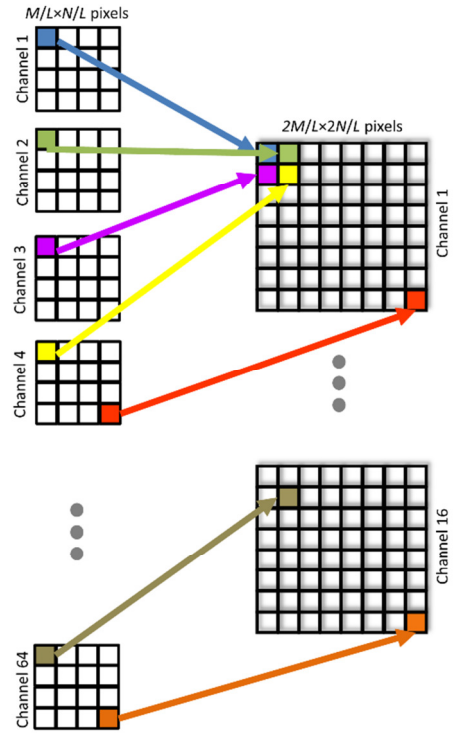
1. Ji, S., Xu, W., Yang, M. & Yu, K. 3D Convolutional Neural Networks for Human Action Recognition. *IEEE Trans. Pattern Anal. Mach. Intell.* **35**, 221–231 (2013).

2. He, K., Zhang, X., Ren, S. & Sun, J. Deep Residual Learning for Image Recognition. in 770–778 (2016).
3. He, K., Zhang, X., Ren, S. & Sun, J. Identity Mappings in Deep Residual Networks. in *Computer Vision – ECCV 2016* (eds. Leibe, B., Matas, J., Sebe, N. & Welling, M.) 630–645 (Springer International Publishing, 2016). doi:10.1007/978-3-319-46493-0\_38
4. Shi, W. *et al.* Real-Time Single Image and Video Super-Resolution Using an Efficient Sub-Pixel Convolutional Neural Network. in 1874–1883 (2016).
5. Kingma, D. & Ba, J. Adam: A Method for Stochastic Optimization. in (2014).
6. Farsiu, S., Robinson, M. D., Elad, M. & Milanfar, P. Fast and Robust Multiframe Super Resolution. *IEEE Trans. Image Process.* **13**, 1327–1344 (2004).
7. Wang, Z., Bovik, A. C., Sheikh, H. R. & Simoncelli, E. P. Image Quality Assessment: From Error Visibility to Structural Similarity. *IEEE Trans. Image Process.* **13**, 600–612 (2004).
8. Press, W. H., Teukolsky, S. A., Vetterling, W. T. & Flannery, B. P. *Numerical Recipes in C (2Nd Ed.): The Art of Scientific Computing.* (Cambridge University Press, 1992).

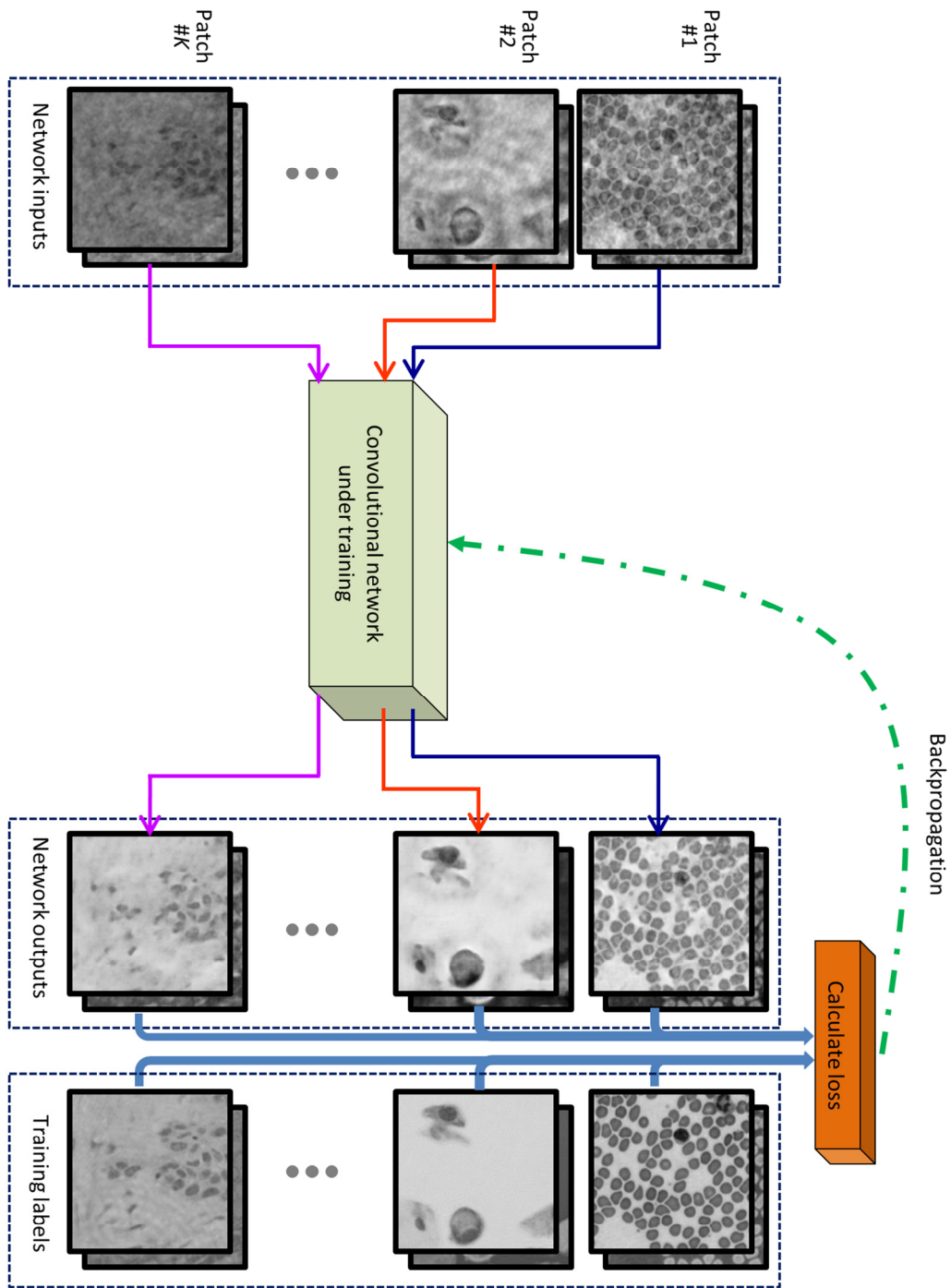
## Supplementary Figures



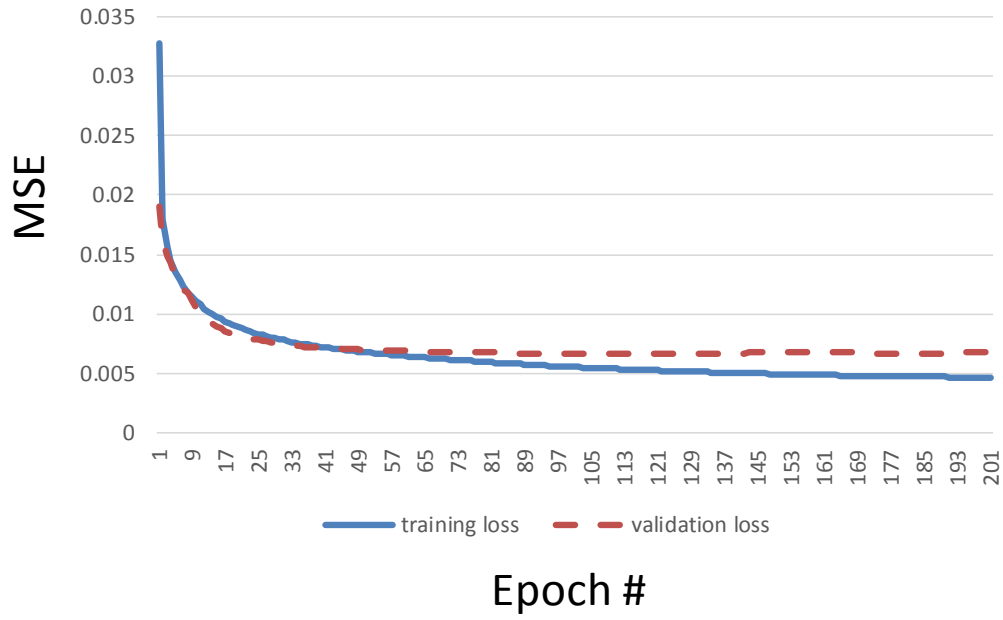
**Supplementary Fig. 1.** Architecture of our deep neural network and its training. The neural network is composed of convolutional layers (i.e., conv layers), upsampling blocks (U/S blocks) and nonlinear activation functions (ReLU). Also see Supplementary Fig. 2.



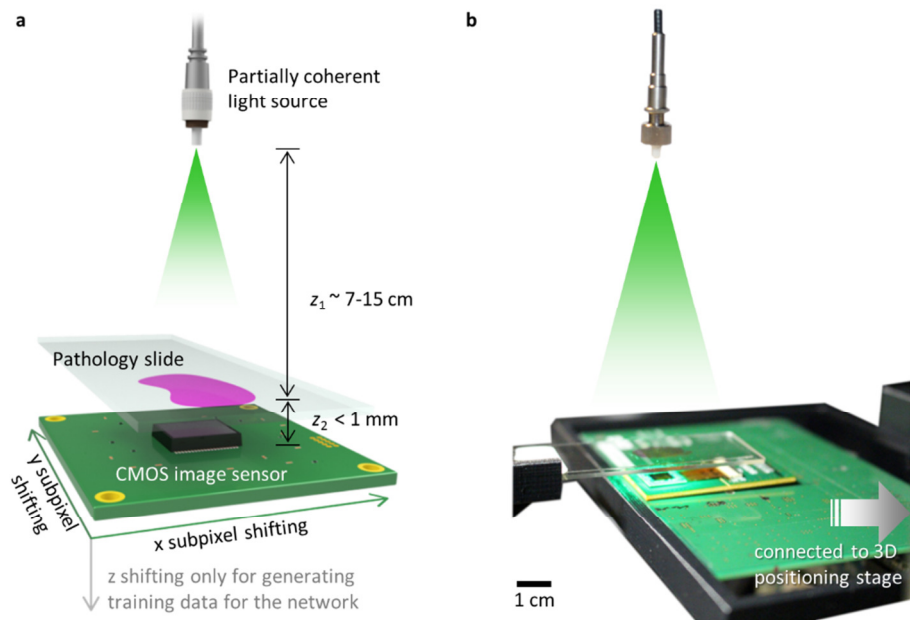
**Supplementary Fig. 2.** Detailed schematics of the upsampling layer of our deep neural network.



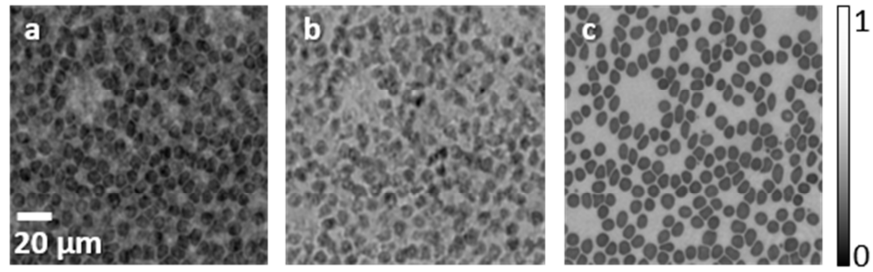
**Supplementary Fig. 3.** Training of the universal deep neural network that can reconstruct different types of objects.



**Supplementary Fig. 4.** Training and validation dataset errors as a function of the number of epochs.



**Supplementary Fig. 5.** Holographic imaging setup. **a**, schematics of the optical set-up. **b**, a photograph of the same setup.



**Supplementary Fig. 6.** The result of feeding a blood smear hologram into a sample type specific network, which was trained with only Pap smear image data. (a) Amplitude of the input blood smear image after free space back-propagation. (b) Pap smear trained network output image (amplitude) in response to (a). (c) Image of the same sample obtained by using the multi-height phase recovery algorithm with  $N_{\text{holo}} = 8$ .